

DNN-based 3D Cloud Retrieval for Variable Solar Illumination and Multiview Spaceborne Imaging

Tamar Klein*, Tom Aizenberg*, Roi Ronen

Abstract—Climate studies often rely on remotely sensed images to retrieve two-dimensional maps of cloud properties. To advance volumetric analysis, we focus on recovering the three-dimensional (3D) heterogeneous extinction coefficient field of shallow clouds using multiview remote sensing data. Climate research requires large-scale worldwide statistics. To enable scalable data processing, previous deep neural networks (DNNs) can infer at spaceborne remote sensing downlink rates. However, prior methods are limited to a fixed solar illumination direction. In this work, we introduce the first scalable DNN-based system for 3D cloud retrieval that accommodates varying camera poses and solar directions. By integrating multiview cloud intensity images with camera poses and solar direction data, we achieve greater flexibility in recovery. Training of the DNN is performed by a novel two-stage scheme to address the high number of degrees of freedom in this problem. Our approach shows substantial improvements over previous state-of-the-art, particularly in handling variations in the sun’s zenith angle.

I. INTRODUCTION

Clouds play a key role in the climate system [13]. They form multi-scale, complex dynamical systems, with a multitude of feedbacks. However, clouds are challenging to resolve or represent in climate models. A finer understanding of clouds is needed. We focus on retrieving the three-dimensional (3D) heterogeneous extinction coefficient field of shallow clouds using multiview remotely sensed data.

To sense clouds volumetrically in 3D, adequate observations are required as a prerequisite. This need led to the CloudCT space mission [12, 14]. Cloud CT includes a coordinated *formation* of ten nano-satellites *simultaneously* imaging a cloud field from multiple directions as illustrated in Fig. 1. In addition to observational improvements, advanced analysis is required.

Recent work [1, 4, 7, 6, 10] showed the potential of cloud scattering tomography, which is a special form of computed tomography (CT). In contrast to X-ray CT, cloud imaging is passive, relying on sun radiation as a source. Image readouts relate *nonlinearly* to volumetric cloud structure by 3D radiative transfer (RT): sunlight reaches the sensor by *scattering*, mainly from cloud droplets and atmospheric particles. To invert the 3D RT, Refs. [1, 4, 7, 6, 10] use iterative-based optimization. However, these methods are slow and unscalable for extracting rich worldwide 3D cloud retrievals.

To address recovery speed, deep neural network (DNN) methods were suggested [9, 11, 2]. DNNs shift the computational load to a *training stage*, making it feasible to analyse large data during inference, at rates comparable to

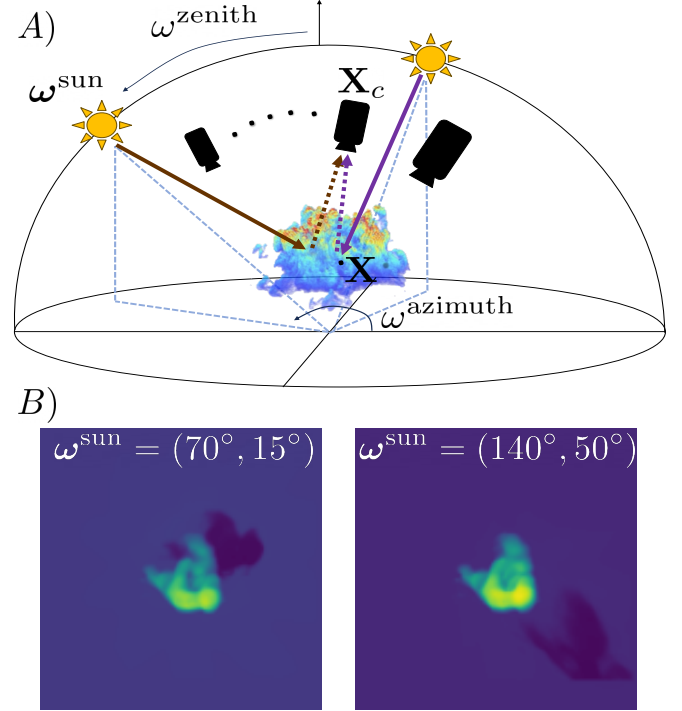


Fig. 1. A) A satellite formation in orbit observes a cloud. The uncontrolled scene is illuminated by the sun in direction $\omega^{\text{sun}} = [\omega^{\text{zenith}}, \omega^{\text{azimuth}}]$. Radiation that reaches a point \mathbf{X} in the atmospheric domain is multiply scattered until sensed by camera sensor at \mathbf{X}_c . B) Cloud single-channel intensity images are shown from the same satellite position. The images change significantly when illuminated from a different direction.

downlink rates typical of spaceborne remote sensing. DNN-based cloud recovery requires training data of cloud volumes and corresponding multiview images. Cloud imaging is performed in an uncontrolled environment (see Fig. 1). Hence, data should include images with an arbitrary incoming sun direction and variable camera poses. The large number of degrees of freedom poses a challenge in acquiring such a large and diverse dataset. Furthermore, even if such a dataset exists, designing and training a DNN system for such complex data is not trivial.

In this work, we address these challenges, presenting Projection Integration for Variable Orientation in Computed Tomography (PIVOT-CT): The first scalable system for 3D cloud retrieval with flexibility in both camera poses and sun direction. We accomplished this by (i) extending the VIP-CT [9] model by incorporating into its decoder the sun direction; and (ii) designing a novel two-stage training scheme. This scheme mitigates the challenge of the many degrees of freedom in our setup.

*These authors contributed equally to this work

II. EXISTING 3D CLOUD LABELED DATA

Prior art [9, 11] for DNN-based cloud tomography requires labeled training data of volumetric clouds and their multiview images. However, obtaining a large in-situ measured database of volumetric cloud fields is infeasible. Therefore, a large *simulated* dataset of 3D cloud fields, termed BOMEX [3], is procured. A cloud scene in this dataset is 1.6×1.6 km wide and 1.2km thick, divided into 32 voxels along each axis. Per voxel, the cloud extinction coefficient β^{true} , single scattering albedo, and phase function are known. Training used 6000 scenes. Testing used 566 scenes.

Per scene, the cloud field extinction coefficients β^{true} and its multiview images are used as a ground-truth labeled pair. Imaging geometry follows the CloudCT space mission: 10 satellites in a string-of-pearls formation, orbiting 500km high. The nearest neighboring satellite distance is 100km. Imaging specifications are detailed in [9]. All synthetic images in the prior database were rendered using the SHDOM [5] RT solver, with a *fixed* solar direction ω_{fixed} , having a zenith angle of $\omega_{\text{fixed}}^{\text{zenith}} = 30^\circ$ and an azimuth angle of $\omega_{\text{fixed}}^{\text{azimuth}} = 135^\circ$.

III. METHODOLOGY

A. Cloud Datasets with Uncontrolled Imaging

Remote sensing of clouds is done in an uncontrolled environment. Satellite positions may be randomly perturbed, and the solar direction

$$\omega^{\text{sun}} = [\omega^{\text{azimuth}}, \omega^{\text{zenith}}], \quad (1)$$

changes constantly relative to the clouds. To generalize learned cloud tomography, training data should include varying imaging settings. Hence, we introduce two new datasets:

BOMEX^{sun}: We randomly sample 1379 and 199 scenes from the BOMEX training and test sets, respectively. Let $\mathcal{U}[a, b]$ be the uniform distribution in the range $[a, b]$. For each training scene β^{true} , we drew ten times the solar direction by $\omega^{\text{azimuth}} \sim \mathcal{U}[0, 360^\circ]$ and $\omega^{\text{zenith}} \sim \mathcal{U}[0, 90^\circ]$. Per sun direction, β^{true} is rendered using SHDOM, to obtain the multiview images under the sampled sun direction.

BOMEX^{sun}_{perturbed}: This dataset follows the previous process to obtain cloud images with varying sun directions. In addition, in this dataset, the camera poses are perturbed: Per camera in the formation, each of the 3D spatial coordinates was randomly translated by $\Delta x, \Delta y, \Delta z \sim \mathcal{U}[-50\text{km}, 50\text{km}]$. This dataset has 845 training scenes and 566 test scenes. For both datasets, sun direction and camera poses are known.

B. PIVOT-CT

The architecture of PIVOT-CT is presented in Fig. 2. PIVOT-CT recovers the extinction coefficient per location of 3D heterogeneous clouds. The inputs to PIVOT-CT are (i) $N^{\text{cam}} = 10$ multiview images of a cloud scene, (ii) a 3D query location vector \mathbf{X} , (iii) a vector of the camera array poses, denoted $\{\mathbf{X}_c\}_{c=1}^{N^{\text{cam}}}$, and (iv) a vector of the sun direction ω^{sun} .

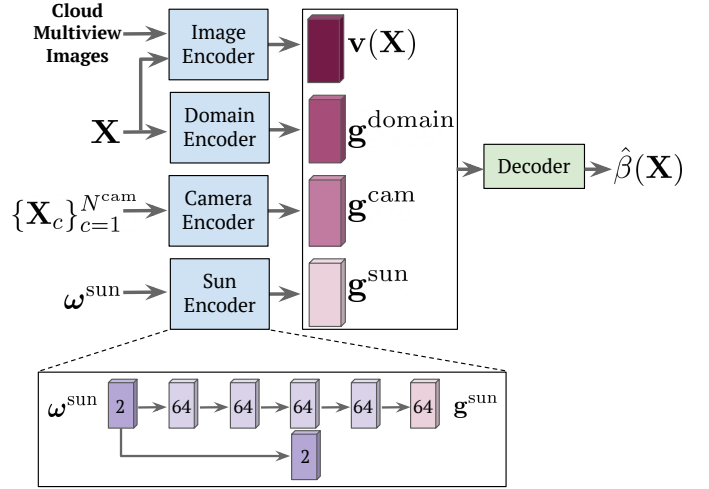


Fig. 2. Architecture of PIVOT-CT. Feature extraction is performed on all images, resulting in a feature vector \mathbf{v} for each atmospheric location \mathbf{X} , corresponding to the image pixels that are the geometric projections of \mathbf{X} . The atmospheric location \mathbf{X} and camera positions $\{\mathbf{X}_c\}_{c=1}^{N^{\text{cam}}}$ are encoded into vectors $\mathbf{g}^{\text{domain}}(\mathbf{X})$ and $\{\mathbf{g}^{\text{cam}}(\mathbf{X}_c)\}_{c=1}^{N^{\text{cam}}}$, respectively. Additionally, the illumination direction ω^{sun} is provided to the system. A zoom-in of the Sun Encoder module is presented. The sun direction $\omega^{\text{sun}} \in \mathbb{R}^2$ is embedded to a vector \mathbf{g}^{sun} by five fully connected layers, each followed by a ReLU activation. These feature vectors are then input into a decoder, which predicts the extinction coefficient $\hat{\beta}(\mathbf{X})$.

Following [9], a convolutional neural network extracts input features of the images. The vector of features is denoted \mathbf{v} . A query location \mathbf{X} in the atmospheric domain can be projected to all camera planes, using the known cameras' properties. The projected points on the camera planes are denoted $\{\mathbf{x}_c\}_{c=1}^{N^{\text{cam}}}$. Hence, per \mathbf{X} , PIVOT-CT samples the features vector \mathbf{v} at corresponding $\{\mathbf{x}_c\}_{c=1}^{N^{\text{cam}}}$. This results in an image feature vector $\mathbf{v}(\mathbf{X})$.

Moreover, the vectors of the location \mathbf{X} , camera positions $\{\mathbf{X}_c\}_{c=1}^{N^{\text{cam}}}$, and sun direction ω^{sun} are processed by three individual fully connected-based DNNs that serve as geometry encoders. This results in corresponding feature vectors $\mathbf{g}^{\text{domain}}(\mathbf{X})$, $\{\mathbf{g}^{\text{cam}}(\mathbf{X}_c)\}_{c=1}^{N^{\text{cam}}}$ and $\mathbf{g}^{\text{sun}}(\omega)$, as seen in Fig. 2.

These learned feature vectors encompass the spatial trends of the scene, influenced primarily by atmospheric physics and radiance. By having these vectors as inputs, our system can handle the changes in viewing geometry and illumination direction. Overall, the encoded vectors are concatenated and fed to a decoder D whose output is the estimated cloud extinction coefficient $\hat{\beta}$ at \mathbf{X} ,

$$\hat{\beta}(\mathbf{X}) = D \left[\mathbf{v}(\mathbf{X}), \mathbf{g}^{\text{domain}}(\mathbf{X}), \{\mathbf{g}^{\text{cam}}(\mathbf{X}_c)\}_{c=1}^{N^{\text{cam}}}, \mathbf{g}^{\text{sun}}(\omega) \right]. \quad (2)$$

The 3D estimated cloud $\hat{\beta}$ is obtained by querying in parallel all locations \mathbf{X} which reside in the 3D cloud convex hull. The hull is estimated by space carving.

C. System Training

Our DNN, PIVOT-CT, processes image data, imaging geometry, and the sun direction. To handle the many degrees of freedom, we employ a two-stage training scheme. In the first stage, PIVOT-CT parameters are randomly initialized. We

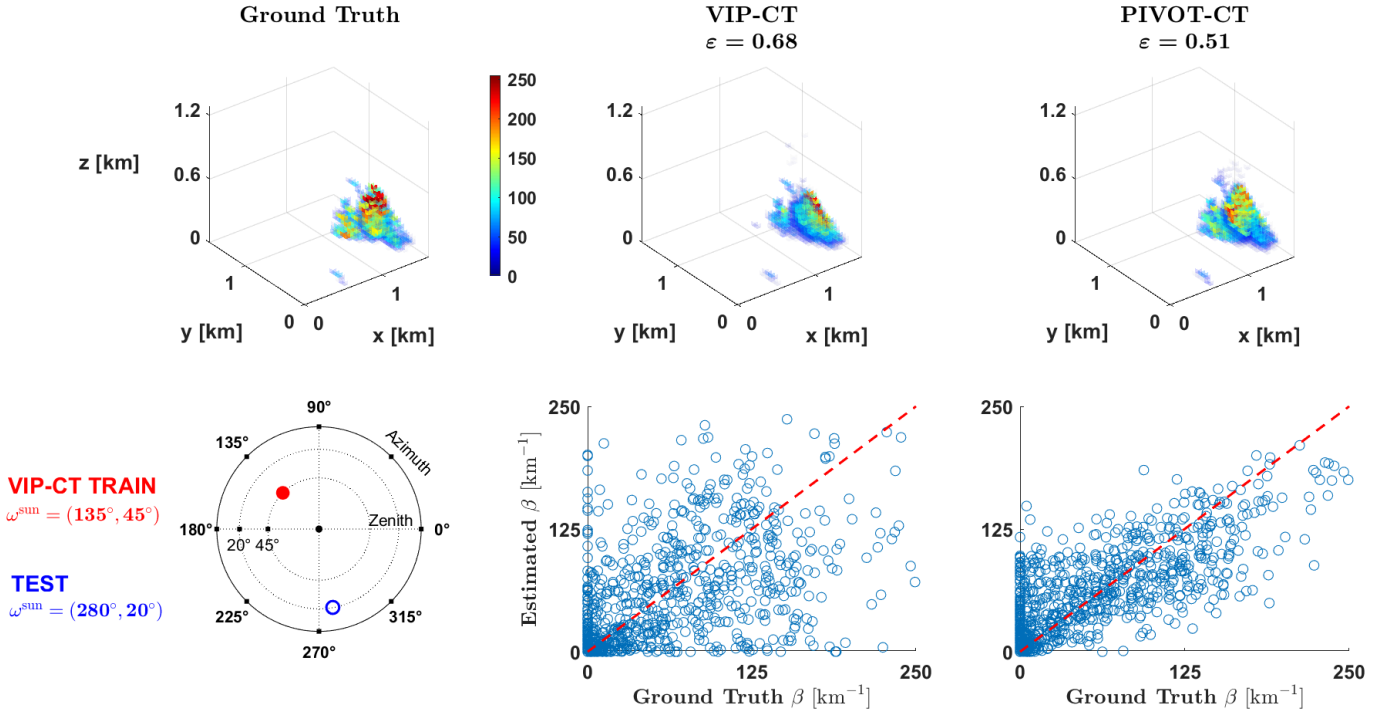


Fig. 3. [Top] Visualizations of a test cloud’s 3D extinction coefficient field and its recovery by VIP-CT and PIVOT-CT (ours). We show the relative error ϵ for each method. [Bottom] An illustration of the solar angle that VIP-CT was trained on and the true test scene solar angle. Scatter plots of the estimated $\hat{\beta}$ compared to the true β^{true} across all voxels, the red dashed line represents optimal recovery.

freeze the sun encoder and set $\mathbf{g}^{\text{sun}} \equiv 0$. The network is trained until convergence on the BOMEX dataset.

In the second training stage, we unfreeze the sun encoder \mathbf{g}^{sun} and train on data with varying sun direction, $\text{BOMEX}_{\text{perturbed}}^{\text{sun}}$ and $\text{BOMEX}^{\text{sun}}$. Network parameters are initialized by the previous stage weights. Here, we freeze the image feature extractor parameters. Empirically, we found this improves performance. We follow [7, 9] and numerically quantify the per scene recovery quality by the relative error metric

$$\epsilon = \left(\|\beta^{\text{true}} - \hat{\beta}\|_1 \right) / \left(\|\beta^{\text{true}}\|_1 \right). \quad (3)$$

We show in Table I that our two-stage training scheme allows PIVOT-CT to better adapt to the complexity in $\text{BOMEX}_{\text{perturbed}}^{\text{sun}}$ and $\text{BOMEX}^{\text{sun}}$ datasets.

Implementation Details: Input sun angles $\omega^{\text{azimuth}}, \omega^{\text{zenith}}$ are rounded to the nearest integer and normalized in the range $[0, 1]$. Following [9], each input image is normalized by the mean and standard deviation of the training data. We train to optimize the relative L2 norm as in [9]. System training stages endured $\approx 4e6$ and $0.25e6$ iterations, respectively. Both stages use an Adam optimizer, a learning rate of $1e-5$, and a weight decay of $1e-5$. An iteration uses 200 randomly sampled query voxels. The system runs on an NVIDIA GeForce RTX 3090 GPU.

IV. RESULTS

Table I compares PIVOT-CT with VIP-CT using the ϵ measure. VIP-CT specializes in a fixed sun direction, thus it outperforms our method by $\approx 11\%$ on the fixed-sun BOMEX

TABLE I
COMPARISON OF VIP-CT AND PIVOT-CT (OURS) USING THE ϵ MEASURE (EQ. 3). OUR METHOD OUTPERFORMS VIP-CT ON DATASETS HAVING A VARYING SUN DIRECTION. TWO-STAGE TRAINING IS VERY HELPFUL.

Method	Two-Stage Strategy	Datasets		
		BOMEX	BOMEX ^{sun}	BOMEX _{perturbed} ^{sun}
VIP-CT	X	35 ± 10	58 ± 28	62 ± 28
PIVOT-CT	X	70 ± 11	62 ± 14	63 ± 14
	✓	45 ± 8	43 ± 12	46 ± 14

dataset. However, in a real-world scenario, where the sun’s pose is random during imaging, PIVOT-CT outperforms VIP-CT on both $\text{BOMEX}^{\text{sun}}$, $\text{BOMEX}_{\text{perturbed}}^{\text{sun}}$ datasets by $\approx 15\%$. Also, PIVOT-CT fails when initialized randomly and directly trained on data with varying sun directions. This shows the benefit of the two-stage training process. Fig. 3 shows a qualitative example from the $\text{BOMEX}_{\text{perturbed}}^{\text{sun}}$ dataset.

Additionally, in Fig. 4, we compare the performance of PIVOT-CT (ours) and VIP-CT as a function of the sun zenith angle. Our method surpasses prior art across all zenith angles, highlighting its robustness.

V. DISCUSSION

We generalize learning-based cloud tomography to enable real-time volumetric retrieval of cloud fields using multi-view imaging from realistic remote sensing. Our proposed method, PIVOT-CT, accommodates variable solar illumination angles and diverse camera array configurations. PIVOT-CT

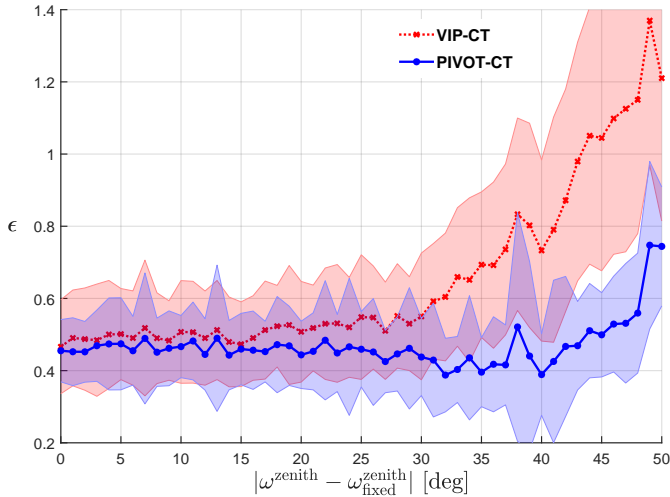


Fig. 4. Comparison of the PIVOT-CT (ours) and VIP-CT systems. This figure shows the ϵ measure (Eq. 3) as a function of the distance between the zenith angle of the test scenes and the zenith angle upon which VIP-CT was trained, $|\omega^{\text{zenith}} - \omega^{\text{zenith}_{\text{fixed}}}|$. The shaded area represents the standard deviation of ϵ . The largest zenith angle difference of 50° stands for the sun at the horizon.

demonstrates significant improvements over the state-of-the-art, particularly in handling variations in the sun’s zenith angle.

As shown in Fig. 4, we observe a notable increase in tomographic error when the sun is near the horizon (90° from nadir). At this position, sunlight is attenuated by atmospheric particles, leading to dimmer cloud images and a reduced signal-to-noise ratio [8]. Additionally, when the sun is directly overhead, all views capture lower-order scattered light, whereas, in oblique sun position, more views capture higher-order scattered light. This results in decreased information content and less accurate retrievals.

Potential extensions of this work include exploring different integrations of the solar illumination direction, the incorporation of multimodal data, such as polarized imaging channels, and retrieval of a parameter vector at each location (e.g., droplet size distribution and density).

VI. ACKNOWLEDGEMENTS

We would like to express our sincere gratitude to Yoav Y. Schechner for his professional advice and Vadim Holodovsky for his help in procuring images. We thank Daniel Yogodin, Ina Talmon, and Jochanan Erez for their technical support. This project has received funding from the European Research Council (ERC) under the European Union’s Horizon 2020 research and innovation programme (CloudCT, grant agreement No. 810370), and the Israel Science Foundation (ISF grant 2514/23).

VII. AUTHORS

Tamar Klein, Technion Israel Institute of Technology
Tom Aizenberg, Technion Israel Institute of Technology
Roi Ronen, Amazon Web Services

REFERENCES

- [1] Amit Aides et al. “Distributed Sky Imaging Radiometry and Tomography”. In: *Proc. IEEE International Conference on Computational Photography*. 2020, pp. 1–12.
- [2] Inbal Kom Betzer et al. “NeMF: Neural Microphysics Fields”. In: *IEEE Transactions on Pattern Analysis and Machine Intelligence* (2024).
- [3] Reuven H. Heiblum et al. “Core and margin in warm convective clouds-Part 1: Core types and evolution during a cloud’s lifetime”. In: *Atmospheric Chemistry and Physics* 19.16 (2019), pp. 10717–10738.
- [4] Vadim Holodovsky et al. “In-situ multi-view multi-scattering stochastic tomography”. In: *Proc. IEEE International Conference on Computational Photography*. 2016, pp. 1–12.
- [5] Aviad Levis, Jesse Loveridge, and Amit Aides. *Pyshdom*. 2020. Available online. <https://github.com/aviadlevis/pyshdom>.
- [6] Aviad Levis, Yoav Y Schechner, and Anthony B Davis. “Multiple-scattering microphysics tomography”. In: *Proc. IEEE/CVF Conference on Computer Vision and Pattern Recognition*. 2017, pp. 6740–6749.
- [7] Aviad Levis et al. “Airborne three-dimensional cloud tomography”. In: *Proc. IEEE/CVF International Conference on Computer Vision*. 2015, pp. 3379–3387.
- [8] Jesse Loveridge et al. “Retrieving 3D distributions of atmospheric particles using Atmospheric Tomography with 3D Radiative Transfer–Part 1: Model description and Jacobian calculation”. In: *Atmospheric Measurement Techniques* 16.7 (2023), pp. 1803–1847.
- [9] Roi Ronen, Vadim Holodovsky, and Yoav Y. Schechner. “Variable Imaging Projection Cloud Scattering Tomography”. In: *IEEE Transactions on Pattern Analysis and Machine Intelligence* (2022), pp. 1–12.
- [10] Roi Ronen, Yoav Y Schechner, and Eshkol Eytan. “4D cloud scattering tomography”. In: *Proceedings of the IEEE/CVF International Conference on Computer Vision*. 2021, pp. 5520–5529.
- [11] Roi Ronen et al. “Learned 3D volumetric recovery of clouds and its uncertainty for climate analysis”. In: *arXiv preprint arXiv:2403.05932* (2024).
- [12] Klaus Schilling, Yoav Y Schechner, and Ilan Koren. “CloudCT - computed tomography of clouds by a small satellite formation”. In: *Proc. IAA Symposium on Small Satellites for Earth Observation*. 2019.
- [13] Kevin E. Trenberth, John T. Fasullo, and Jeffrey Kiehl. “Earth’s Global Energy Budget”. In: *Bulletin of the American Meteorological Society* 90.3 (2009), pp. 311–324.
- [14] Masada Tzabari et al. “CloudCT 3D volumetric tomography: considerations for imager preference, comparing visible light, short-wave infrared, and polarized imagers”. In: *Polarization Science and Remote Sensing X*. 2021, p. 4.